AGU PUBLICATIONS

JGR

Journal of Geophysical Research: Earth Surface

RESEARCH ARTICLE
10.1002/2013JF002849

Key Points:
- Rift-related seismicity controlled by mechanical heterogeneity
- Back projection reveals that seismic deformation is continuous in region
- Spacing of rift-transverse crevasses controls the timing of seismic swarms

Supporting Information:
- Readme
- Figure S1
- Movie S1

Correspondence to:
D. S. Heeszel,
david.heeszel@nrc.gov

Citation:
Heeszel, D. S., H. A. Fricker, J. N. Bassis, S. O'Neel, and F. Walter (2014), Seismicity within a propagating ice shelf rift: The relationship between icequake locations and ice shelf structure, *J. Geophys. Res. Earth Surf.*, *119*, 731–744, doi:10.1002/2013JF002849.

Received 8 MAY 2013
Accepted 17 JAN 2014
Accepted article online 21 JAN 2014
Published online 2 APR 2014

Seismicity within a propagating ice shelf rift: The relationship between icequake locations and ice shelf structure

David S. Heeszel[1], Helen A. Fricker[1], Jeremy N. Bassis[2], Shad O'Neel[3], and Fabian Walter[4]

[1]Scripps Institution of Oceanography, University of California, San Diego, La Jolla, California, USA, [2]Department of Atmospheric, Oceanic and Space Sciences, University of Michigan, Ann Arbor, Michigan, USA, [3]Alaska Science Center, United States Geological Survey, Anchorage, Alaska, USA, [4]Institut des Sciences de la Terre, Université de Grenoble I, CNRS, Grenoble, France

Abstract Iceberg calving is a dominant mass loss mechanism for Antarctic ice shelves, second only to basal melting. An important process involved in calving is the initiation and propagation of through-penetrating fractures called rifts; however, the mechanisms controlling rift propagation remain poorly understood. To investigate the mechanics of ice shelf rifting, we analyzed seismicity associated with a propagating rift tip on the Amery Ice Shelf, using data collected during the austral summers of 2004–2007. We apply a suite of passive seismological techniques including icequake locations, back projection, and moment tensor inversion. We confirm previous results that show ice shelf rifting is characterized by periods of relative quiescence punctuated by swarms of intense seismicity of 1 to 3 h. Even during periods of quiescence, we find significant deformation around the rift tip. Moment tensors, calculated for a subset of the largest icequakes ($M_w > -2.0$) located near the rift tip, show steeply dipping fault planes, horizontal or shallowly plunging stress orientations, and often have a significant volumetric component. They also reveal that much of the observed seismicity is limited to the upper 50 m of the ice shelf. This suggests a complex system of deformation that involves the propagating rift, the region behind the rift tip, and a system of rift-transverse crevasses. Small-scale variations in the mechanical structure of the ice shelf, especially rift-transverse crevasses and accreted marine ice, play an important role in modulating the rate and location of seismicity associated with the propagating ice shelf rifts.

1. Introduction

Two processes are responsible for most of the mass loss from Antarctic ice shelves: iceberg calving and basal melting [*Rignot et al.*, 2013]. Enhanced basal melting from changing atmospheric and oceanic forcing is implicated as the major cause of recent increased mass flux from many ice shelves [*Pritchard et al.*, 2012]. Occasional large calving events are easily monitored by repeat satellite imagery, but calving is a sporadic process [*Fricker et al.*, 2002; *Joughin and MacAyeal*, 2005; *Lazzara et al.*, 1999], and the multidecadal timescales on which large iceberg calving events recur are much longer than the existing satellite record [*Fricker et al.*, 2002; *Jacobs et al.*, 1986; *Lazzara et al.*, 1999]. Additionally, the temporal sampling and spatial resolution of satellite imagery are insufficient to resolve the short timescale processes involved. Therefore, little is known about the mechanics of tabular iceberg calving.

The precursor to the detachment of a large tabular iceberg from an ice shelf is the formation and subsequent propagation of through-cutting rifts, which sever the entire ice thickness. These rifts eventually become the boundaries where icebergs separate from the ice shelf. Understanding rift propagation is required to understand the process of iceberg calving. Identifying and locating fracturing events using passive seismic observations provide a powerful means to study the physical processes associated with calving [*Bartholomaus et al.*, 2012; *Bassis et al.*, 2005, 2007; *Richardson et al.*, 2010, 2012]. Because seismic waves also contain information that constrain rupture mechanics [e.g., *Walter et al.*, 2009; *Wiens et al.*, 2008], passive seismology-derived results provide information about the temporal variability in the stress state of the ice shelf on time and spatial scales shorter than is possible to determine with satellite monitoring.

In this study we reprocess seismic data acquired between 2004 and 2007 to study the ice shelf rifting process on the Amery Ice Shelf (AIS) in East Antarctica [*Bassis et al.*, 2005, 2007, 2008]. Like other large Antarctic ice

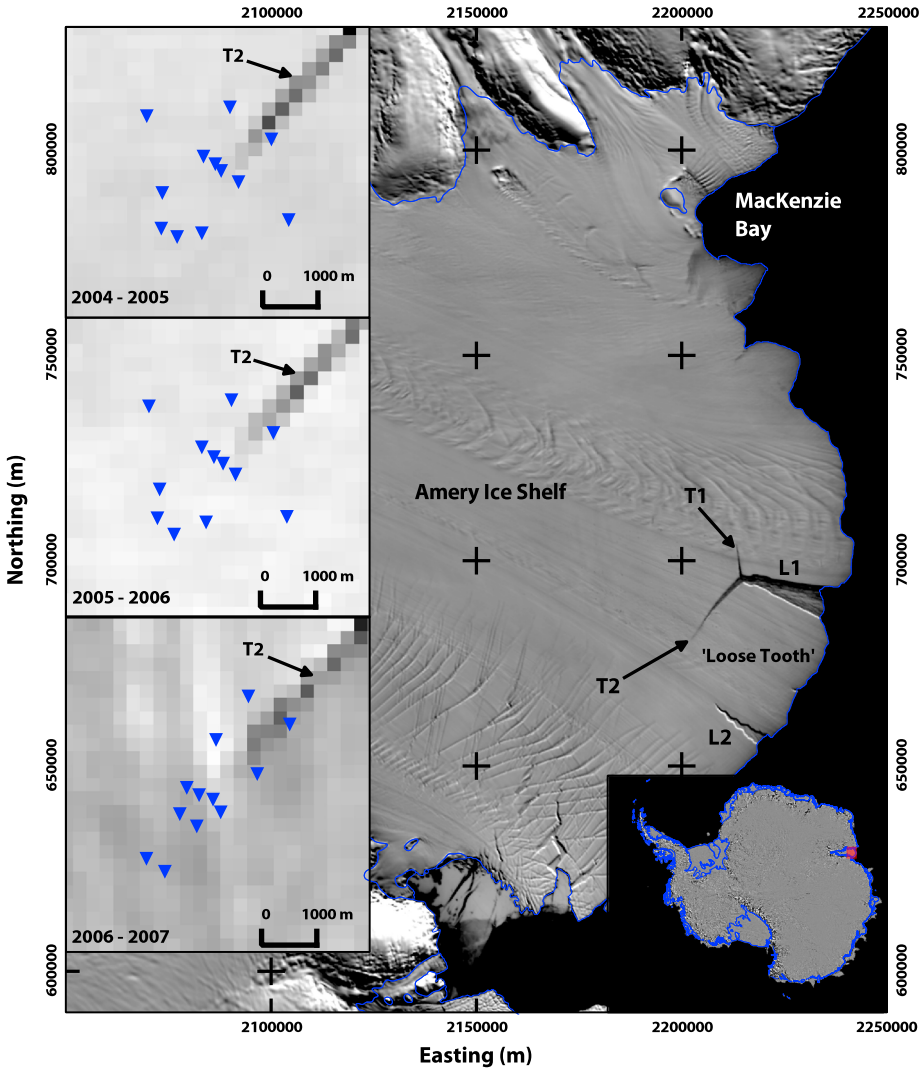

Figure 1. Location of the "Loose Tooth" of the Amery Ice Shelf. L1 and L2 rifts are longitudinal to flow, and T1 and T2 are transverse. During the 2004–2007 austral summers, an array of 12 short-period seismic stations was deployed around the propagating tip of the T2 rift with an aperture of approximately 3 km (blue triangles shown on insets at left). Each season's array is depicted on a MODIS image from the corresponding period that is contrast-stretched to highlight the rift. T2 appears as a large dark line of pixels entering the array region from the upper right. MODIS mosaic of Antarctica [*Haran et al.*, 2005] with study region highlighted by red box (lower right). All maps are plotted in Antarctic Polar Stereographic with true scale at 71°S.

shelves, the AIS calves infrequently and produces large tabular icebergs every 50–60 years [*Budd*, 1966; *Fricker et al.*, 2002]. The AIS is unusual, however, because it has numerous through-cutting rifts extending along flow (longitudinally) from the calving front into the ice shelf [*Fricker et al.*, 2002; *Walker et al.*, 2013]. The formation of these rifts is believed to be primarily the result of glaciological stress [*Bassis et al.*, 2005, 2008; *Fricker et al.*, 2005a]. One longitudinal rift (L1; Figure 1) propagates upstream from the ice front and branches into two transverse rifts, forming a triple junction labeled T1 and T2 in Figure 1. We focus on the tip of the T2 rift, which, at the time of the seismic deployment, was propagating at an average speed of 4−6 m/d [*Fricker et al.*, 2005b] through a field of crevasses oriented longitudinal to flow (transverse to the T2 rift) [*Bassis et al.*, 2007]. In this area the AIS has a total ice thickness of ~300 m with a marine ice layer ~118 m thick [*Craven et al.*, 2009; *Fricker et al.*, 2001], and the ice flow velocity is ~1300 m/a [*Joughin*, 2002; *Young and Hyland*, 2002].

Previous analyses of the AIS seismic data focused on the occurrence of "swarms" of seismic activity and their relationship to possible forcing mechanisms for rift propagation [*Bassis et al.*, 2005, 2007, 2008]. In those studies, icequake locations were determined by applying a lower detection threshold than are presented

here resulting in more icequakes detected at fewer stations. Observed seismic swarms, characterized by periods of intense seismic activity accompanied rift propagation episodes and were concentrated at the rift tip. They typically lasted 1 to 3 h and had a recurrence interval of 10–24 days [*Bassis et al*., 2005, 2007]. Investigations of possible external forcing mechanisms by *Bassis et al*. [2008] found little evidence for correlation with temperature variations, wind forcing, sea ice (used as a proxy for ocean swell), tidal variability, or the impact of tsunamis. Strain triangles for a GPS network collocated with the seismic network revealed that the strain induced by the propagating rift tip is confined to the region immediately in front of the propagating rift and that strain elsewhere is dominated by the background glaciological stress [*Bassis et al*., 2007].

In this paper, we analyze icequake locations and moment tensors to better constrain the mechanics of, and controls on, rift propagation within the AIS. We apply two different algorithms to identify and locate distinct icequakes. First, we utilize *P* wave onset times to constrain discrete event locations using a more sophisticated approach than was applied previously. Second, we have performed back projection of continuous seismic energy to locate seismicity for time periods when identifying discrete events was impossible [*Xu et al*., 2009]. Back projection enables us to image how seismicity changes on varying spatial and temporal scales. In addition to icequake locations, we investigated the source mechanisms associated with well-located icequakes, revealing the mode of deformation, the orientation of stress within the ice shelf, and the energy released by individual icequakes. By combining these methods, the distribution of seismicity and its relationship to the propagation of an active ice shelf rift is better constrained.

2. Data

Seismic data used in this study were collected by an array of 12 seismometers deployed around the observed tip of the T2 rift on AIS (Figure 1). Data were collected over a period of between 1 and 3 months during the austral summers of 2004–2005, 2005–2006, and 2006–2007 (a total of 182 days). Station configurations consisted of Mark Products L28 three-component, short-period seismometers (4.5 Hz natural frequency) and Quanterra Q330 digital acquisition systems with GPS timing. One exception to this configuration occurred during the 2006–2007 field season when two Guralp CMG-40T medium bandwidth (30 s long-period corner) seismometers were deployed in addition to 10 short-period sensors. Data were collected continuously with a sampling frequency of 200 Hz. For each of the three seasonal deployments, the array had a maximum aperture of 3–3.5 km depending on the geometry of the propagating rift at the time of observation (Figure 1).

3. Methods

3.1. Icequake Locations

We determined final icequake locations using a multistep process, in which we refined the location of the icequake at each stage. We performed initial icequake location using the traditional earthquake location technique of picking onset times for seismic phases and performing an inversion that minimizes misfit between observed arrival times and those predicted by an appropriate velocity model [*Stein and Wysession*, 2003]. We initially identified onset times automatically using a short-time average/long-time average (STA/LTA) event detector and grid search algorithm [*Quinlan et al*., 1996]. The STA/LTA detector compares the average amplitude of waveforms in a short-time window to that of a longtime window. When the STA/LTA ratio exceeds a predefined value, a potential phase arrival is cataloged. These arrivals are compared to a precompiled 3-D grid of possible locations using traveltimes calculated from a 1-D velocity model. The velocity model is based on active source studies of the AIS [*McMahon and Lackie*, 2006] (Figure 2). Though the *P* wave velocity of 1375 m/s reported by *McMahon and Lackie* [2006] is unreasonably low, it has little effect on resulting icequake location or focal mechanisms. Events are cataloged only if a sufficient number of phase arrivals (eight) fit a location on the grid and have *P* wave arrival residuals of less than 2 s. We subsequently reviewed these events for additional arrivals and relocated them using the GENLOC software package [*Pavlis et al*., 2004], in which we conducted a damped least squares inversion of traveltime residuals for icequake locations using the location found in the previous stage as the starting location.

The accuracy of our icequake locations are limited because we use a 1-D velocity model in a region known to have significant lateral variations in seismic velocity due to different structure across the ice shelf (e.g., crevassed regions and the mélange-filled rift). We improved the accuracy using a relative relocation routine based on the Joint Hypocentroidal Decomposition (JHD) method [*Jordan and Sverdrup*, 1981]. The JHD

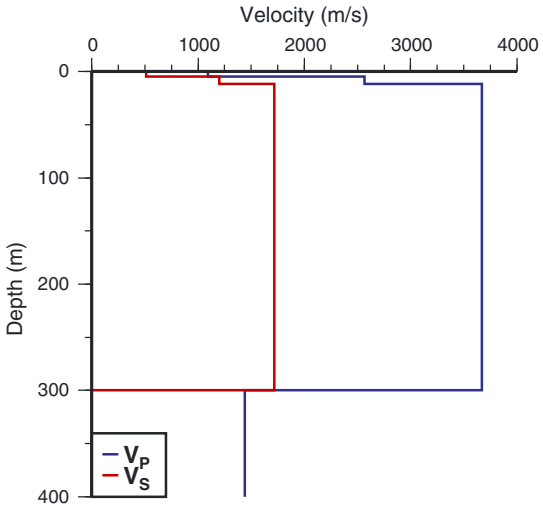

Figure 2. Seismic velocity model used for event location and moment tensor inversion after active source studies on the AIS [*McMahon and Lackie*, 2006].

method has proven effective at removing path biases associated with a 3-D velocity structure on various length scales in seismicity studies in a variety of seismological settings [*Emry et al*., 2011; *Heeszel et al*., 2008; *Korger and Schlindwein*, 2012; *Wiens et al*., 1994]. The algorithm removes path biases introduced by representing the Earth's 3-D velocity structure as 1-D. The icequake location problem is separated into two parts: (i) a hypocentroid location representing the average location of all events in a region and (ii) a cluster vector, which describes the location of events relative to the hypocentroid. We improve the cluster vector by minimizing traveltime residuals for icequakes with traveltime data at a common subset of stations. The algorithm then updates the location of the hypocentroid using all available traveltime residuals and the updated cluster vectors. By solving iteratively for the cluster vector and the hypocentroid location, we were able to improve absolute locations and individual events relative to the hypocentroid.

The icequakes detected from our three 12 station networks (Figure 1) typically had very small or nonexistent *S* wave arrivals; therefore, we used only *P* wave onset time in our analysis. The inclusion of only *P* wave data limits depth resolution, so we fixed the depth in our inversion to the value determined by the initial location algorithm. This assigned depth represents a compromise between uncertainties in location and velocity model in the initial icequake location, with the caveat that icequake depth be less than the total ice shelf thickness of 300 m [*Fricker et al*., 2005b]. While the initial location grid search requires only eight arrivals, we limit our final icequake catalog to events with 10 or more arrivals having small location errors, and we analyze each season's data independently to improve stability in the inversion.

3.2. Swarm Locations—Back Projection

While prior analyses of seismic data collected around the T2 rift focus on the occurrence of swarms, accurately identifying and locating all seismicity associated with these swarms by picking the onset time of discrete phases is difficult due to events overlapping one another [*Bassis et al*., 2005, 2007]. In addition, we performed back projection on continuous data during swarm and nonswarm periods. We adapt the teleseismic method of *Xu et al*. [2009] to the problem of local icequake location in the near field (i.e., within the seismic array). First, we aligned seismograms and stacked them based on predicted traveltimes from a grid of potential source locations. This produced a map of the spatial variability of beam power, or stack amplitude, from which the most probable location was determined. Rather than modeling incident energy at nearby stations as a plane wave, we assumed a curved wave front expanding outward from the source region. Results from this method indicate how beam power varies as a function of frequency and velocity, in addition to location. We limited our back-projection analysis to the pass band (3–7 Hz) which contains coherent surface wave energy to accommodate the method's computational intensity.

Using a moving-window analysis with 3 s time windows and a 2 s overlap, we constructed a time record of icequake locations during swarm periods. This provides a second-by-second image of seismicity within the source region. Within each individual 3 s window, we performed multichannel cross correlation to determine lag times between all station pairs [*VanDecar and Crosson*, 1990]. Geographic back-projection analysis identified the maximum in beam power as the most likely source for that time window. During periods of low seismic activity, numerous peaks existed for a single time window, which was considered a "null" event. During an icequake, however, one single, geographically isolated peak in beam power appeared, which we interpreted as the event epicenter for that time window. We combined the event epicenters for a 2 h period to construct a normalized frequency-location map of seismicity (Figure 4).

3.3. Moment Tensors

Moment tensor analysis of icequakes permits a quantitative analysis of seismic sources on an event-by-event basis. The method places constraints on the faulting mechanism, orientation of principle stress axes, and energy release of each icequake. Moment tensors are calculated by comparing a suite (vertical dip slip, vertical strike slip, 45° dip slip, and explosion) of synthetic seismograms (Green's functions) to observed waveforms. These generic Green's functions can be combined linearly to construct any potential moment tensor. Moment tensor analysis has recently been applied to mountain glaciers [*Walter et al*., 2009, 2010]. These recent investigations focus on a constrained moment tensor, which assumes an extensional crack opening combined with a shear dislocation, or fault. The method, termed "crack + dc," relies on a grid search algorithm that assumes the orientation of the extensional crack is perpendicular to the shear dislocation [*Minson et al*., 2007]. Similar source types were found when considering either the unconstrained moment tensor inversion or the constrained inversion. We perform full moment tensor inversions to capture the full range of possible mechanisms and not bias our results. This is particularly important in the mélange-filled rift, where nonrifting mechanisms, e.g., pieces of ice breaking off from the rift wall or blocks shifting against one another within the rift, are likely to occur.

For all events with acceptable location using the JHD method, full moment tensor inversions were used to investigate the source mechanisms [*Dreger*, 2003; *Minson and Dreger*, 2008]. We precomputed Green's functions using the reflectivity method [*Saikia*, 1994]. The velocity model used to calculate Green's functions is the same used for icequake location (Figure 2). We removed instrument response to displacement and band-pass filtered the data from 3 Hz to 10 Hz. This frequency band represents a compromise between determining the moment tensor and uncertainties in velocity structure. Higher-frequency data provide better constraints on source mechanisms but increase scattering effects and introduce uncertainties in small-scale velocity structure that decrease the stability of the inversion [*Stein and Wysession*, 2003]. We limited our station selection to stations less than 1 km away from the event. In order to constrain the depths of observed icequakes, we conducted a grid search over depth in 10 m increments between 10 m and 300 m depth. Only inversions with variance reduction exceeding 40% are reported here. The selection of a minimum variance reduction of 40% is subjective but is based on comparison of marginal waveform fits with very poor ones. Reported icequake focal depths are those associated with the maximum variance reduction.

4. Results

4.1. Icequake Locations

We located 965 icequakes with the JHD technique (Figure 3); locations were dominated by events occurring along the rift axis, either at the rift tip or near the rift walls. The next most common events are associated with crevasses oriented transversely to the rift. Epicenters for these rift-transverse icequakes were less well constrained due to their location outside the central region of the array and their relatively low-amplitude arrivals. During swarm periods, icequake locations determined from discrete phase arrivals were concentrated near the rift tip.

We report uncertainty estimates for detected icequake locations as ellipsoids with axis lengths and orientations (Table 1 and Figure S1 in the supporting information). Median uncertainties are significantly lower than mean uncertainties due to the presence of a small number of outlier events with high uncertainties. Additionally, a systematic offset parallel to the flow direction exists between the mapped rift location and observed seismicity (Figure 3). This offset is explained by the JHD method incompletely correcting for 3-D velocity structure across the region and from advection of ice (approximately 1300 m/a) [*Joughin*, 2002; *Young and Hyland*, 2002], as this introduces a systematic downstream shift as each season evolves. The effect of increased seismic energy release on icequake location is highlighted by continuous back-projection results (Figure 4). We compare results from two, 2 h periods; one during a swarm (high seismicity), and one during a time in which no icequakes are detected using the STA/LTA method (low-seismicity, or "quiet" period). Back-projection results for the two periods are similar in their spatial distribution of seismicity. They reveal relative increase in seismicity on the rift wall and on rift-transverse crevasses during the quiet period (Figure 4b); which is consistent with results determined using traveltimes alone. Location errors for back projection are difficult to assess quantitatively. However, results derived from applying the back-projection method to active source data on the Whillans Ice Stream in West Antarctica suggest that location errors are

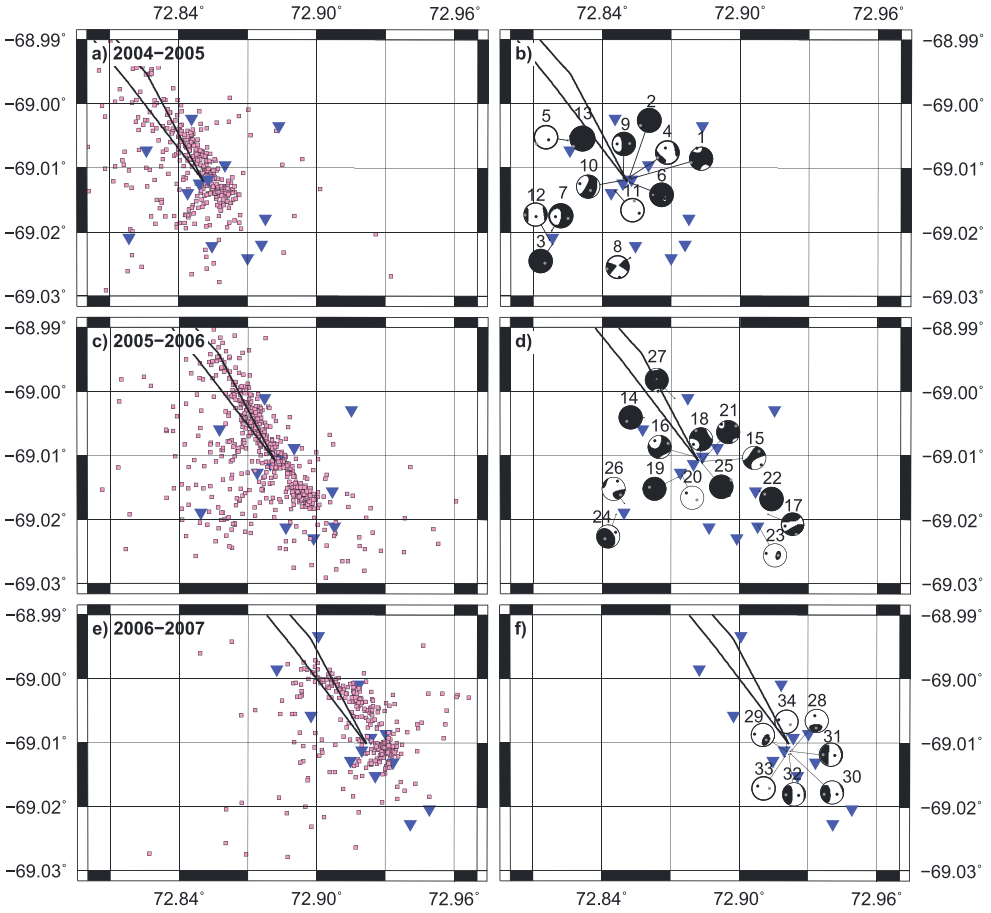

Figure 3. (a, c, and e) Map of icequake locations and (b, d, and f) moment tensors determined during the 2004–2005 (Figures 3a and 3b), 2005–2006 (Figures 3c and 3d), and 2006–2007 (Figures 3e and 3f) field seasons. Violet squares are locations determined by JHD method. Full moment tensors are plotted along with primary stress axes (σ_1 in black and σ_3 in grey) for each icequake. Advection of rift from ice flow is evident as location of array and rift shifts from left to right through time. Approximate rift outline is plotted as a heavy black line, and station locations are inverted blue triangles.

approximately 150 m, which is a 68% reduction in location error relative to the median uncertainty using the JHD method (Table 1).

4.2. Moment Tensors

We determined acceptable moment tensor solutions for 34 of the 965 icequakes (Figure 3 and Table 2). Moment tensor results for well-located icequakes often had a significant isotropic (volumetric) component (Figure 5), indicative for substantial deviations from pure shear faults. The depth grid search for each moment tensor inversion (Figure 6) showed that icequake depths were largely limited to the upper 50 m of the ice shelf (Table 2). Stress orientations for moment tensors were generally oriented horizontally or are shallowly plunging (Table 2). This is consistent with other studies that suggest that englacial stress controls propagation of ice shelf rifts [*Bassis et al.*, 2008; *Hulbe et al.*, 2010; *Joughin and MacAyeal*, 2005].

Table 1. Mean Uncertainty Ellipses With 2σ Bounds and Corresponding Medians for All Icequakes Detected During Each Season

	Mean Values		Median Values	
Season	Semiminor Axis (km)	Semimajor Axis (km)	Semiminor Axis (km)	Semimajor Axis (km)
2004–2005	0.43 ± 0.51	1.51 ± 7.94	0.35	0.40
2005–2006	0.47 ± 0.48	1.43 ± 4.69	0.40	0.47
2006–2007	0.53 ± 0.64	1.30 ± 2.59	0.39	0.84

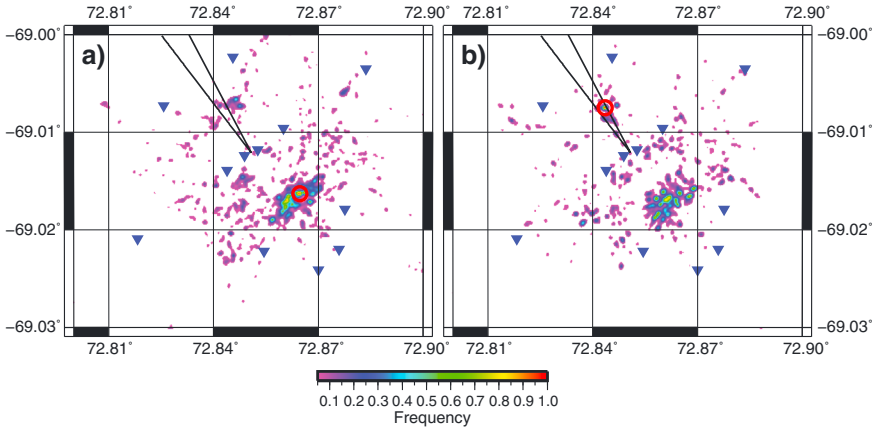

Figure 4. Frequency normalized location results during (a) a swarm and (b) a quiet period. Overall pattern of seismicity is similar for both periods. Location of peak seismicity during each period is circled.

Our moment tensor results were not as high quality as typically reported for tectonic earthquakes or in mountain glaciers (Figure 6). This is due to a number of factors including instrument noise due to wind, shallow burial, limits of instrumentation, and unmodeled source complexities. There also exist complexities in the velocity structure, which our simple-layered velocity model does not capture, such as the heavily crevassed surface and the mélange-filled rift. To ensure that moment tensors results calculated here are reasonable, we calculated a synthetic moment tensor with 30% Gaussian noise added. The inversion results indicated that we recovered the magnitude, orientation of the primary stress axis, and isotropic component with a reasonable degree of certainty (Figure 7). Therefore, given the consistent nature of the moment tensor solutions and their stability (Figure 6b), we are confident in making qualitative interpretations about the nature of the moment tensors and their implications for deformation in the region.

Moment tensor results revealed that energy release associated with icequakes is small, approximately 5.6×10^7 N m ($M_w = -1.14$), and often includes a significant isotropic component to the observed seismicity (Figure 5). If we assume Lamé parameters $\lambda = 6.55 \times 10^9$ N/m^2 and $\mu = 3.55 \times 10^9$ N/m^2 ($E = 9.40 \times 10^9$ N/m^2, $\nu = 0.32$) [*Gammon et al.*, 1983] then the volumetric expansion of the rift, from an icequake with an isotropic moment of 1.26×10^8 N m (event 33, Table 2), is 0.014 m^3 [*Müller*, 2001].

5. Discussion

5.1. Link Between Swarms and Rift Processes

Previous work shows that seismicity and rift propagation in the study region are punctuated by rift tip swarms occurring at irregular intervals that are not well correlated with external forcing mechanisms such as tides, winds, or temperatures [*Bassis et al.*, 2008]. We find evidence for continuous deformation at the rift tip during nonswarm periods, and moment tensor results reveal that there is significant spatial and temporal variation in the orientation of stresses in the rift system (Figure 2 and Table 2). However, many of the tension axes plunge relatively shallowly (20 have a tension axis plunge of less than 45°). This is consistent with the hypothesis that background stresses dominate the process of ice shelf rifting [*Joughin and MacAyeal*, 2005]. GPS measurements for the 2005–2006 field season indicate that the along-flow velocity during the deployment period is nearly constant [*Bassis et al.*, 2007]. Icequake locations determined during swarms are nearly identical to those occurring during interswarm periods, although the relative frequency of rift tip seismicity increases during swarm periods. These results suggest that seismic swarms are a symptom of mechanical variations within the rift system that allows for relatively larger and/or more frequent icequakes at the rift tip. This leads to an interesting question: if swarms are not a result of an external forcing mechanism, what controls their timing and location?

One possible control on the occurrence of seismic swarms is that spatial heterogeneities in the mechanical properties of ice shelf affect the temporal seismic potential of the rift. We note the presence of the seismicity

Journal of Geophysical Research: Earth Surface
10.1002/2013JF002849

Table 2. Moment Tensor Parameters for Icequakes Plotted in Figures 3 and 5[a]

				Moment Tensor[b]										T[e] = σ_3		P[f] = σ_1	
Event	Latitude	Longitude	Depth (m)	M_{xx}	M_{xy}	M_{xz}	M_{yy}	M_{yz}	M_{zz}	M_0 (10^7 N m)	M_w	%Isotropic[c]	%VR[d]	Plunge	Azimuth	Plunge	Azimuth
								2004–2005									
1	−69.0117	72.8526	40	−0.04	0.21	0.02	0.42	0.05	0.16	0.32	−1.73	37	47	9	69	0	159
2	−69.0115	72.8517	30	2.83	2.18	1.65	5.85	0.35	2.32	3.30	−1.05	53	45	13	59	40	160
3	−69.0219	72.8182	220	1.14	0.18	0.41	1.04	−0.76	1.64	0.94	−1.41	58	40	56	295	33	122
4	−69.0114	72.8519	20	−1.42	1.62	1.90	1.13	−0.44	−3.47	3.40	−1.04	27	40	5	62	54	159
5	−69.0057	72.8249	10	−2.05	0.94	−0.38	−1.44	0.47	−3.83	1.70	−1.24	59	55	3	55	67	318
6	−69.0123	72.852	20	0.81	0.19	−0.38	3.58	1.55	0.81	2.20	−1.17	44	52	53	12	37	193
7	−69.0198	72.8179	190	4.11	−3.08	0.32	3.21	−8.72	−0.64	9.50	−0.74	19	49	76	353	3	95
8	−69.024	72.8521	80	−3.69	1.02	−0.63	1.78	0.20	−0.16	3.00	−1.08	19	42	2	80	10	350
9	−69.0116	72.8492	10	0.28	0.01	−0.04	0.23	−0.66	0.30	0.66	−1.52	29	49	46	265	44	88
10	−69.0118	72.8509	10	0.09	0.09	0.12	−0.20	−0.19	0.15	0.30	−1.75	4	45	59	329	25	110
11	−69.0136	72.8456	10	−0.59	0.57	−0.93	−3.10	−0.02	−2.82	1.60	−1.26	58	53	19	191	35	295
12	−69.0212	72.8169	20	−0.94	0.12	−0.24	0.77	0.10	−1.80	1.30	−1.32	33	57	2	86	75	349
13	−69.005	72.8258	90	17.50	3.72	0.38	17.62	−0.07	13.61	4.00	−1.00	80	56	2	45	55	138
								2005–2006									
14	−69.0041	72.8581	30	2.99	2.52	1.28	4.21	0.39	6.79	3.40	−1.04	58	57	54	43	8	144
15	−69.0109	72.8836	10	−0.21	0.83	−0.40	−0.34	0.14	0.26	0.93	−1.42	10	43	30	216	15	314
16	−69.0103	72.8817	10	−0.13	1.18	0.66	1.05	−1.02	0.29	1.80	−1.23	19	59	22	249	32	143
17	−69.0192	72.9123	130	14.24	−5.49	−0.20	−1.19	−1.09	−1.60	9.80	−0.74	28	40	0	342	29	73
18	−69.0101	72.8828	10	1.01	−1.05	−0.48	0.04	−0.34	0.75	1.30	−1.32	32	58	14	151	19	56
19	−69.0134	72.8731	10	0.71	0.03	−0.24	0.70	0.78	1.22	0.86	−1.44	51	44	54	106	36	289
20	−69.0131	72.8749	10	−0.21	−0.02	0.06	−0.17	−0.11	−0.10	0.13	−1.99	55	58	52	297	38	127
21	−69.0109	72.8832	20	1.05	1.61	−0.23	1.56	−0.62	1.04	1.70	−1.24	41	45	17	231	10	138
22	−69.0155	72.9085	200	9.19	−2.15	−4.90	12.90	3.47	2.98	8.10	−0.79	51	51	23	124	62	339
23	−69.0209	72.9079	10	−0.20	0.09	0.03	−0.48	−0.23	−0.03	0.33	−1.72	41	51	67	266	22	104
24	−69.0192	72.8461	20	0.02	0.09	0.36	0.05	0.51	0.98	0.76	−1.48	32	40	56	63	23	192
25	−69.0111	72.8833	50	7.89	4.51	−0.36	10.36	−0.15	8.86	4.70	−0.95	66	47	4	233	3	323
26	−69.0175	72.8496	10	−0.35	−0.43	0.35	−0.02	0.00	−0.24	0.58	−1.55	26	43	21	311	29	209
27	−69.0011	72.8716	40	−0.10	0.11	−0.08	0.65	0.04	0.95	0.54	−1.58	48	40	83	121	5	352
								2006–2007									
28	−69.0111	72.923	10	−2.99	2.50	12.37	−8.20	−1.04	−9.02	13.00	−0.65	34	40	38	6	50	161
29	−69.0113	72.9207	10	−2.79	−1.44	7.95	−24.69	−14.10	−6.04	20.00	−0.53	36	80	46	331	29	96
30	−69.0117	72.9224	10	−4.73	2.91	0.49	6.37	11.35	−5.12	13.00	−0.65	8	49	31	80	56	286
31	−69.0113	72.9222	20	−2.92	1.29	−1.75	12.55	18.45	−13.13	23.00	−0.49	5	67	28	89	62	283
32	−69.0118	72.9217	10	−2.09	0.83	−0.02	4.40	7.48	−2.34	8.20	−0.79	0	69	33	86	57	280
33	−69.0121	72.9200	10	−23.18	4.81	5.60	−26.21	−24.97	−23.89	26.00	−0.45	49	63	47	273	42	110
34	−69.0107	72.9207	10	−9.15	3.84	5.33	−31.05	−16.83	−11.78	20.00	−0.53	46	43	57	309	30	102

[a]Event number corresponds to Figure 3.
[b]Moment tensor parameters follow Kanamori convention [*Kanamori and Given*, 1981].
[c]Amount of moment tensor that is volumetric.
[d]Reduction is misfit between observed and modeled waveforms.
[e]Orientation of minimum compressive stress.
[f]Orientation of maximum compressive stress.

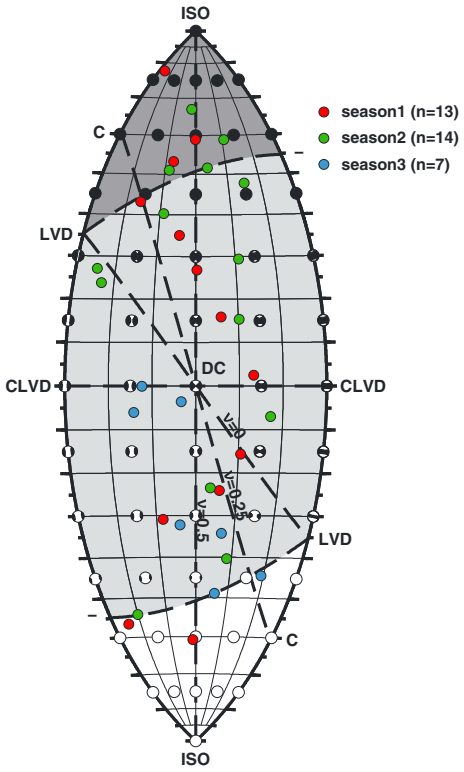

Figure 5. Moment tensor solutions plotted on fundamental lune [*Tape and Tape*, 2012]. The color corresponds to the season during which each event occurs. Events in upper shaded region have entirely extensional moment tensors. Events in lower white region have entirely compressional moment tensors. The distance along the *y* axis represents the isotropic, or volumetric, component. Distance along the *x* axis represents the deviation of the moment tensor for a purely shear faulting mechanism. Reference moment tensors for standard fault types are plotted as black and white "beach balls." Fault parameters for three values of Poisson's ratio (ν) are plotted as lines. Abbreviations on fundamental lune represent specific faulting end-members: ISO (isotropic), C (crack), LVD (linear vector dipole), CLVD (compensated linear vector dipole), and DC (double couple).

associated with rift-transverse crevasses (Figures 3 and 4). This system of crevasses likely plays some role in controlling the overall pattern of seismicity associated with the propagation of the rift. We suggest that when the rift intersects a rift-transverse crevasse, additional stress is required to propagate across the crevasse. Stress builds aseismically at the intersection of the rift tip and crevasse or is expressed as small icequakes occurring at the tips of the crevasse. These small icequakes are difficult to identify using the STA/LTA detection routine due to their small amplitude and larger distance from the center of the array. This state exists until enough stress accumulates within the crevasse to overcome the fracture toughness of the down-rift crevasse wall, leading to intense seismicity (Figure 8). Rift-transverse crevasse spacing is approximately 100 m [*Bassis et al.*, 2005]. At a propagation velocity of 4–6 m/d [*Fricker et al.*, 2005a], the rift tip requires 16–25 days to propagate from one crevasse to the next, which is similar to the time elapsed between observed swarms (10–24 days). Back-projection results for several minutes during swarm periods provide evidence for this mode of deformation (Figure 9 and Movie S1). During a swarm, periods of elevated seismicity at the rift tip are followed by a period of increased seismicity on the network of rift-transverse crevasses. The lower level of seismic energy release during the period immediately prior to and following the seismic burst at the rift tip is evident in the increased geographic distribution of high-integrated beam power. During the period of intense seismicity at the rift tip, only a small region of the search area near the rift tip becomes illuminated (Figure 9 and Movie S1). Following the burst of seismicity at the rift tip, we observe a more distributed pattern in beam power, but one that is more coherent than occurs prior to the rift tip burst. Moment tensor results also support extension occurring in areas of the study region located well away from the rift tip (Figures 3b and 3d). Additionally, photographs taken during fieldwork indicate that this mode of deformation is actively occurring (Figure 10). When the rift propagates across a crevasse, the location of the rift tip is observed to move horizontally (jump) along the crevasse.

Stress transfer can explain the interaction between transverse crevassing and propagating rift. Similar to what has been modeled in tectonic regimes [*Kase and Kuge*, 1998], stress is transferred from the rift that intersects with the crevasse to the crevasse tip. The fracture toughness of the crevasse wall opposite the propagating tip would then control rift propagation. When the crevasse wall fails, the sudden extension of the rift produces a swarm of seismicity.

While the rift penetrates the entire ice shelf thickness, 82% of the observed moment tensors occur in the upper 50 m of the ice shelf (Table 2). A central question, then, is how surface fracturing can control propagation of a through-cutting rift. A possible explanation is that the seismic signature of rift propagation is depth dependent. While transverse crevasses can influence rift dynamics and seismicity at the surface, they may have little influence on rift propagation below the surface-crevassing zone. At these depths the rift may

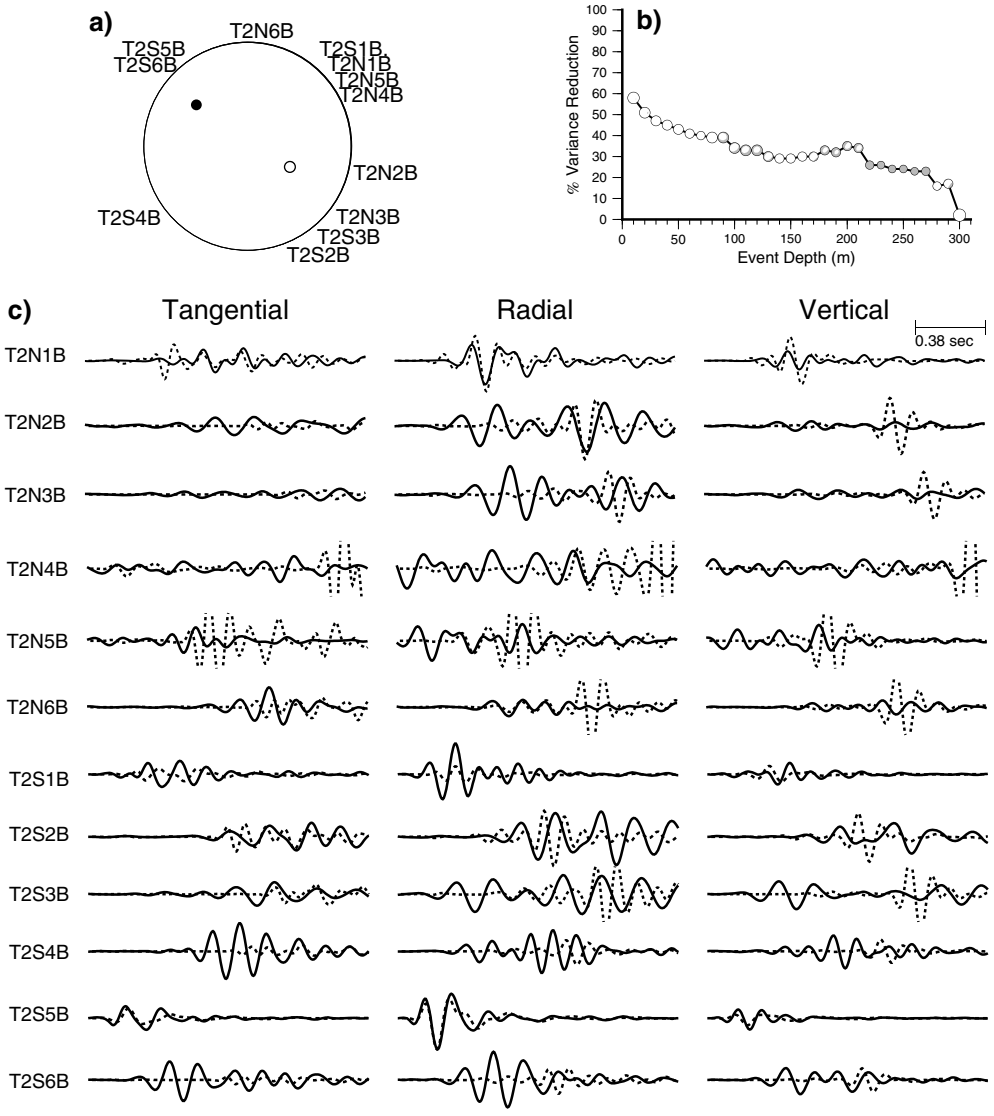

Figure 6. (a) Moment tensor solution and (b) variance reduction as a function of depth and (c) waveform comparison for best fit depth solution for event 20 (Table 2 and Figure 3). Station locations are plotted relative to event location (Figure 6a). Moment tensor solution is dominantly compressive with shallowly plunging σ_1 (black) and σ_3 (white with black outline) axes. Maximum variance reduction occurs at a depth of 10 m and declines steadily with increasing depth. Waveforms (Figure 6c) are normalized to the peak amplitude for each station. Solid line is observed; dashed is synthetic. Total length of seismic traces is 1.52 s.

propagate aseismically, and episodic seismicity at the surface may indicate that the rift tip at or near the surface is "catching up" with the rift at depth.

5.2. Role of Marine Ice

In the study region the basal marine ice layer is ~ 118 m thick [*Fricker et al*., 2001], which accounts for ~40% of the entire ice thickness. It is not known what effect propagation of the rift through such a region has on seismic activity, but it is thought that marine ice behaves in a manner that is less likely to fracture than meteoric ice [*Craven et al*., 2009; *Jansen et al*., 2010]. Temperature has been shown recently to play a significant role in the behavior of marine ice [*Dierckx and Tison*, 2013]. The distribution of temperature within the marine layer ice under the AIS is likely to play some role in the release of seismic energy from the rift; unfortunately, this is poorly constrained. Furthermore, most spatial mappings of marine ice thickness are based on satellite techniques [*Fricker et al*., 2001; *Khazendar et al*., 2009] which have kilometer-scale resolution and fail to capture the variation on length scales relevant to seismicity. Since marine ice is warmer or less

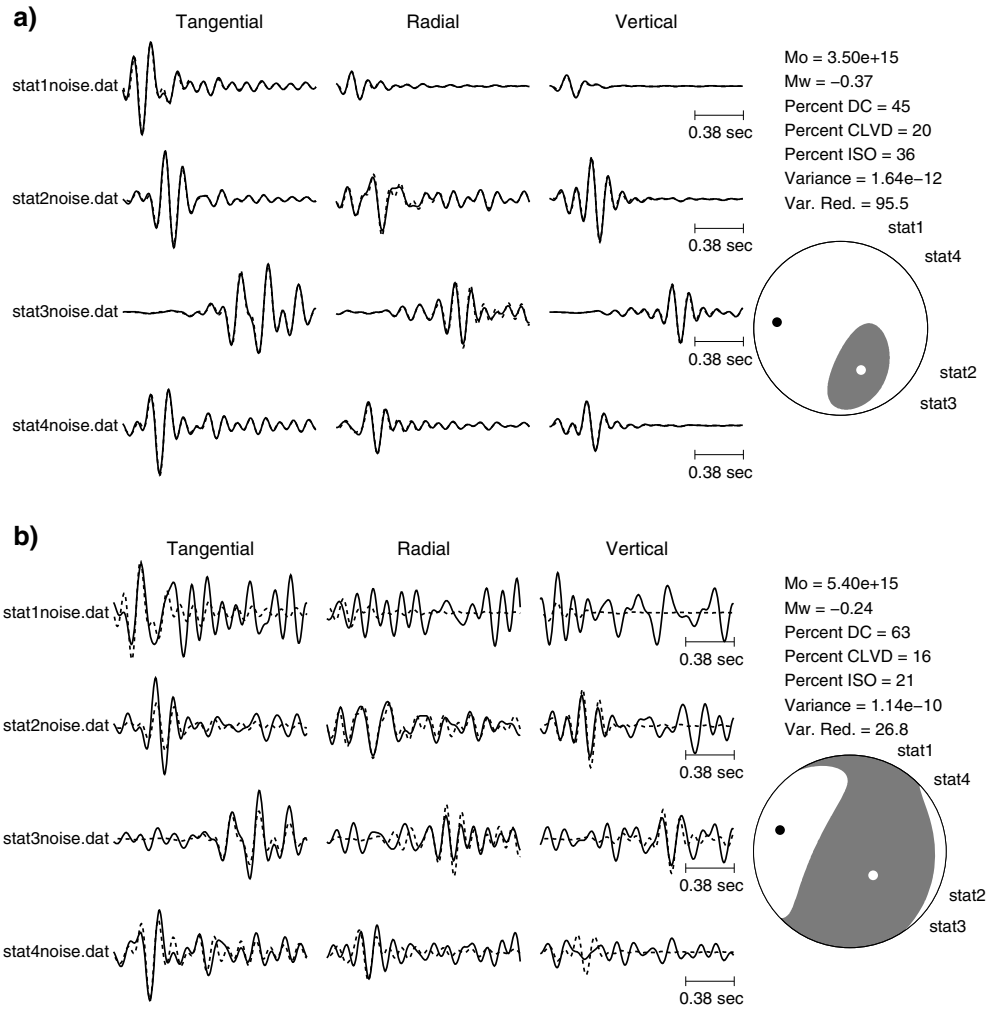

Figure 7. Comparison of moment tensors determined (a) without and (b) with 30% Gaussian noise. In the absence of noise, we recover the input moment tensor nearly perfectly (variance reduction of 95.5%) (Figure 7a).

viscous than meteoric ice, it may inhibit fracture processes; therefore, lower portions of the ice shelf may be less seismically active than the upper, colder, meteoric portion of the ice shelf. The few icequakes for which we calculate moment tensors in the lower portion of the ice shelf often have higher seismic moments than those near the surface. This is consistent with a region that inhibits fracture. A larger stress would be required to induce fracture, resulting in a marginally larger icequake.

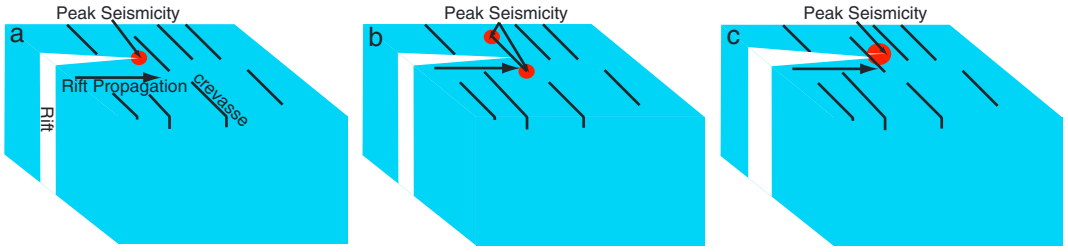

Figure 8. Cartoon visualization of seismicity associated with propagation of T2 rift through a field of rift-transverse crevasses, depicting the following sequence of events: (a) rift propagates in absence of crevasse, and seismicity is concentrated at rift tip; (b) rift intercepts a transverse crevasse, and seismicity moves to tips of crevasse and is smaller in amplitude; and (c) sufficient stress has built up to allow the rift to propagate through the crevasse, and seismicity concentrates near the rift tip resulting in a swarm of icequakes.

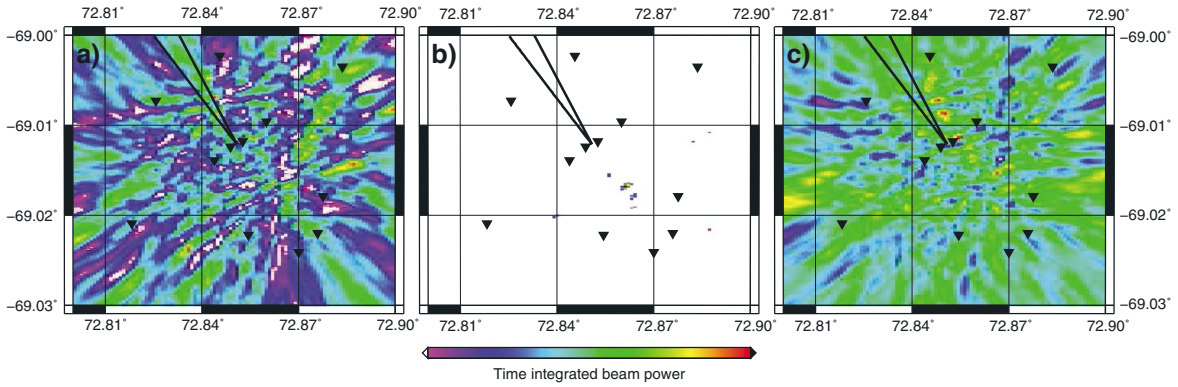

Figure 9. Time-integrated beam power maps for three 1 min periods during a seismic swarm that occurs during the 2004–2005 field season: (a) 1 min immediately prior to a burst at the rift tip, (b) the minute during which seismicity was concentrated at the rift tip, and (c) the minute following. Each time slice is normalized to the peak-integrated beam power for that period.

5.3. Potential External Forcing

Existing fracture and marine ice distribution depend on variations in the mechanical properties of the AIS to control the occurrence of seismic swarms. No sudden changes in rift propagation velocity are required to generate different levels of observes seismicity. However, the possibility of unrecognized first order controls on rift propagation and seismic swarms cannot be ignored. *Bassis et al*. [2008] analyzed the effect that various potential external forcing mechanisms has on stress within the AIS and found that no single forcing mechanism is able to overcome the glaciological stress in the region, a result consistent with studies of the Ronne Ice Shelf [*Hulbe et al*., 2010]. It is possible that an external forcing mechanism or some combination of forcing mechanisms combined with one of the above mechanical controls could influence the occurrence of seismic swarms. Since relatively little evidence indicates that outside forcing mechanisms control the occurrence of swarms in the region, we favor one of the proposed simple mechanical controls as an explanation for their occurrence.

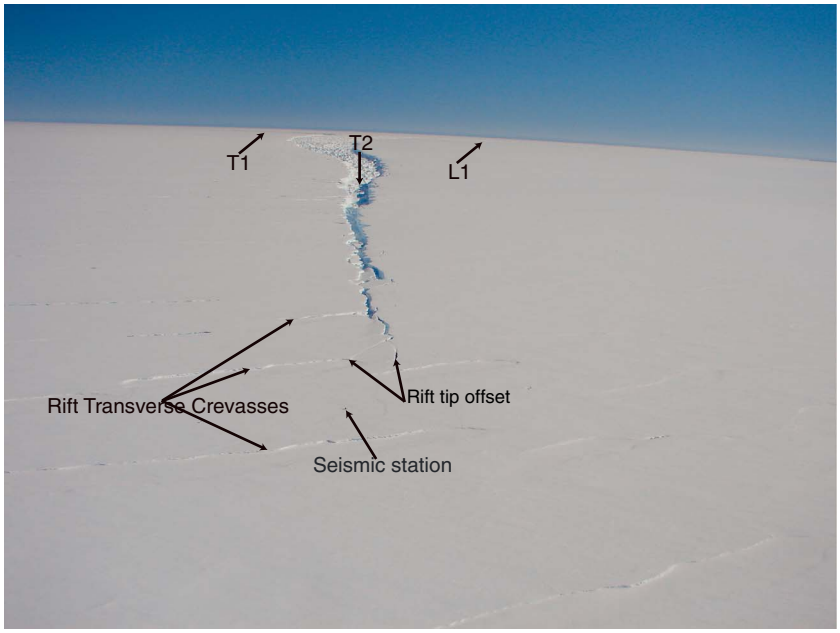

Figure 10. Photograph of the propagating T2 rift taken 14 February 2007. Rift-transverse crevasses are apparent in the region of the rift tip, as is the offset of the rift associated with propagation across the crevasse. Splaying of the rift behind the crevasse produces large blocks of ice that eventually form the rift mélange. Major ice shelf rifts and a seismic station are labeled. Photograph provided by James Behrens.

6. Conclusions

Using a suite of passive seismological methods, we have reprocessed three seasons (2004–2007) of passive seismic data acquired at the propagating tip of a rift on the Amery Ice Shelf. As in past studies, we find that ice shelf seismicity is characterized by relative quiescence punctuated by brief periods of intense seismicity. However, back-projection results reveal that even during periods of relative quiescence, significant seismicity occurs in the study region. Back projection also reveals seismicity associated with a network of rift-transverse crevasses. These results indicate that seismogenic deformation of the region around the rift tip is continuous and that seismicity rates are dependent on the mechanical structure of the ice shelf. Moment tensor inversions for selected icequakes reveal that stress in the system is largely controlled by background glaciological stress, consistent with modeling work of propagating fractures [*Hulbe et al*., 2010; *Joughin and MacAyeal*, 2005]. Moment tensors also reveal that seismicity is concentrated in the upper 50 m of the ice shelf, consistent with the observed depths of crevasses in the region. When considered together, these results indicate that periods of intense seismicity, or swarms, are likely the result of mechanical heterogeneities in the ice shelf. While surface crevasses likely play a significant role in the occurrence of seismic swarms, marine ice may inhibit seismicity, making understanding of rift propagation from surface observations alone difficult. A more detailed study of the mechanical and physical variation within the region of the propagating rift tip is required to constrain the manner in which the rifts propagate over the thickness of the ice shelf.

Acknowledgments

Funding for this research was provided by NSF grants OPP-0739769 and OPP-0337838. J.N. Bassis was supported by NASA grant NNX10AB216G, NSF CAREER grant ANT-114085, and NSF grant EAGER-NSF-ARC. S. O'Neel was supported by the USGS Climate and Land Use Change Mission Area. D.S. Heeszel was partially supported by the Cecil H. and Ida B. Green Foundation at IGGP, Scripps Institution of Oceanography. The Program for Array Seismic Studies of the Continental Lithosphere (PASSCAL), part of the Incorporated Research Institutions for Seismology (IRIS), provided seismic equipment. Archived data are available at IRIS online (http://www.iris.edu/hq). The Australian Antarctic Division provided logistical support for fieldwork. We thank Jacob Walter and four anonymous reviewers for helpful comments that improved the clarity of this manuscript. We thank William and Carl Tape for making their lune plotting scripts available.

References

Bartholomaus, T. C., C. F. Larsen, S. O'Neel, and M. E. West (2012), Calving seismicity from iceberg-sea surface interactions, *J. Geophys. Res.*, *117*, F04029, doi:10.1029/2012JF002513.

Bassis, J. N., R. Coleman, H. A. Fricker, and J. B. Minster (2005), Episodic propagation of a rift on the Amery Ice Shelf, East Antarctica, *Geophys. Res. Lett.*, *32*, L06502, doi:10.1029/2004GL022048.

Bassis, J. N., H. A. Fricker, R. Coleman, Y. Bock, J. Behrens, D. Darnell, M. Okal, and J. B. Minster (2007), Seismicity and deformation associated with ice-shelf rift propagation, *J. Glaciol.*, *53*(183), 523–536.

Bassis, J. N., H. A. Fricker, R. Coleman, and J. B. Minster (2008), An investigation into the forces that drive ice-shelf rift propagation on the Amery Ice Shelf, East Antarctica, *J. Glaciol.*, *54*(184), 17–27.

Budd, W. (1966), The dynamics of the Amery Ice Shelf, *J. Glaciol.*, *6*(45), 335–358.

Craven, M., I. Allison, H. A. Fricker, and R. Warner (2009), Properties of a marine ice layer under the Amery Ice Shelf, East Antarctica, *J. Glaciol.*, *55*(192), 717–728.

Dierckx, M., and J.-L. Tison (2013), Marine ice deformation experiments: An empirical validation of creep parameters, *Geophys. Res. Lett.*, *40*, 134–138, doi:10.1029/2012GL054197.

Dreger, D. S. (2003), TDMT_INV: Time domain seismic moment tensor Inversion, in *International Handbook of Earthquake and Engineering Seismology*, edited by W. H. K. Lee et al., p. 1627, Academic Press, London.

Emry, E. L., D. A. Wiens, H. Shiobara, and H. Sugioka (2011), Seismogenic characteristics of the Northern Mariana shallow thrust zone from local array data, *Geochem. Geophys. Geosyst.*, *12*, Q12008, doi:10.1029/2011GC003853.

Fricker, H. A., S. Popov, I. Allison, and N. Young (2001), Distribution of marine ice beneath the Amery Ice Shelf, *Geophys. Res. Lett.*, *28*(11), 2241–2244.

Fricker, H. A., N. W. Young, I. Allison, and R. Coleman (2002), Iceberg calving from the Amery Ice Shelf, East Antarctica, *Ann. Glaciol.*, *34*, 241–246.

Fricker, H. A., J. N. Bassis, B. Minster, and D. R. MacAyeal (2005a), ICESat's new perspective on ice shelf rifts: The vertical dimension, *Geophys. Res. Lett.*, *32*, L23S08, doi:10.1029/2005GL025070.

Fricker, H. A., N. W. Young, R. Coleman, J. N. Bassis, and J. B. Minster (2005b), Multi-year monitoring of rift propagation on the Amery Ice Shelf, East Antarctica, *Geophys. Res. Lett.*, *32*, L02502, doi:10.1029/2004GL021036.

Gammon, P. H., H. Kiefte, M. J. Clouter, and W. W. Denner (1983), Elastic constants of artificial and natural ice samples by Brillouin spectroscopy, *J. Glaciol.*, *29*(103), 433–460.

Haran, T., J. Bohlander, T. Scambos, and M. Fahnestock (2005), *MODIS Mosaic of Antarctica (MOA) Image Map*, National Snow and Ice Data Center Digital Media, Boulder, CO, U.S.A.

Heeszel, D. S., D. A. Wiens, H. Shiobara, and H. Sugioka (2008), Earthquake evidence for along-arc extension in the Mariana Islands, *Geochem. Geophys. Geosyst.*, *9*, Q12X03, doi:10.1029/2008GC002186.

Hulbe, C. L., C. LeDoux, and K. Cruikshank (2010), Propagation of long fractures in the Ronne Ice Shelf, Antarctica, investigated using a numerical model of fracture propagation, *J. Glaciol.*, *57*(97), 459–472.

Jacobs, S. S., D. R. MacAyeal, and J. L. Ardai Jr. (1986), The recent advance of the Ross Ice Shelf, Antarctica, *J. Glaciol.*, *32*(112), 464–474.

Jansen, D., B. Kulessa, P. R. Sammonds, A. Luckman, E. C. King, and N. F. Glasser (2010), Present stability of the Larsen C ice shelf, Antarctic Peninsula, *J. Glaciol.*, *56*(198), 593–600, doi:10.3189/002214310793146223.

Jordan, T. H., and K. A. Sverdrup (1981), Teleseismic location techniques and their application to earthquake clusters in the south-central Pacific, *Bull. Seismol. Soc. Am.*, *71*(4), 1105–1130.

Joughin, I. (2002), Ice-sheet velocity mapping: A combined interferometric and speckle-tracking approach, *Ann. Glaciol.*, *34*, 195–201.

Joughin, I., and D. MacAyeal (2005), Calving of large tabular icebergs from ice shelf rift systems, *Geophys. Res. Lett.*, *32*, L02501, doi:10.1029/2004GL020978.

Kanamori, H., and J. W. Given (1981), Use of long-period surface waves for rapid determination of earthquake-source parameters, *Phys. Earth Planet. Inter.*, *27*, 8–31.

Kase, Y., and K. Kuge (1998), Numerical simulation of spontaneous rupture processes on two non-coplanar faults: The effect of geometry on fault interaction, *Geophys. J. Int.*, *135*, 911–922.

Khazendar, A., E. Rignot, and E. Larour (2009), Roles of marine ice, rheology, and fracture in the flow and stability of the Brunt/Stancomb-Wills Ice Shelf, *J. Geophys. Res.*, *114*, F04007, doi:10.1029/2008JF001124.

Korger, E. I. M., and V. Schlindwein (2012), Performance of localization algorithms for teleseismic mid-ocean ridge earthquakes: The 1999 Gakkel Ridge earthquake swarm and its geological interpretation, *Geophys. J. Int.*, *188*, 613–625, doi:10.1111/j.1365-246X.2011.05282.x.

Lazzara, M. A., K. C. Jezek, T. A. Scambos, D. R. MacAyeal, and C. J. Van Der Veen (1999), On the recent calving of icebergs from the Ross Ice Shelf, *Polar Geogr.*, *23*(3), 201–212, doi:10.1080/10889370802175937.

McMahon, K. L., and M. A. Lackie (2006), Seismic reflection studies of the Amery Ice Shelf, East Antarctica: Delineating meteoric and marine ice, *Geophys. J. Int.*, *166*(2), 757–766, doi:10.1111/j.1365-246X.2006.03043.x.

Minson, S. E., and D. S. Dreger (2008), Stable inversions for complete moment tensors, *Geophys. J. Int.*, *174*, 585–592, doi:10.1111/j.1365-246X.2008.03797.x.

Minson, S. E., D. S. Dreger, R. Burgmann, H. Kanamori, and K. M. Larson (2007), Seismically and geodetically determined nondouble-couple source mechanisms from the 2000 Miyakejima volcanic earthquake swarm, *J. Geophys. Res.*, *112*, B10308, doi:10.1029/2006JB004847.

Müller, G. (2001), Volume change of seismic sources from moment tensors, *Bull. Seismol. Soc. Am.*, *91*(4), 880–884, doi:10.1785/0120000261.

Pavlis, G. L., F. Vernon, D. Harvey, and D. Quinlan (2004), The generalized earthquake-location (GENLOC) package: An earthquake-location library, *Comput. Geosci.*, *30*, 1079–1091, doi:10.1016/j.cageo.2004.06.010.

Pritchard, H. D., S. R. M. Ligtenberg, H. A. Fricker, D. G. Vaughan, M. R. van den Broeke, and L. Padman (2012), Antarctic ice-sheet loss driven by basal melting of ice shelves, *Nature*, *484*, 502–505, doi:10.1038/nature10968.

Quinlan, D. M., D. Harvey, and G. Wagner (1996), Datascope seismic application package, *Seismol. Res. Lett.*, *67*(2), 51.

Richardson, J. P., G. P. Waite, K. A. FitzGerald, and W. D. Pennington (2010), Characteristics of seismic and acoustic signals produced by calving, Bering Glacier, Alaska, *Geophys. Res. Lett.*, *37*, L03503, doi:10.1029/2009GL041113.

Richardson, J. P., G. P. Waite, W. D. Pennington, R. M. Turpening, and J. M. Robinson (2012), Icequake locations and discrimination of source and path effects with small aperture arrays, Bering Glacier terminus, AK, *J. Geophys. Res.*, *117*, F04013, doi:10.1029/2012JF002405.

Rignot, E., S. Jacobs, J. Mouginot, and B. Scheuchl (2013), Ice-shelf melting around Antarctica, *Science*, *341*, 266–270, doi:10.1126/science.1235798.

Saikia, C. K. (1994), Modified frequency-wavenumber algorithm for regional seismograms using Filon's quadrature: Modelling of L_g waves in eastern North America, *Geophys. J. Int.*, *118*, 142–158.

Stein, S., and M. Wysession (2003), *An Introduction to Seismology, Earthquakes, and Earth Structure*, pp. 498, Blackwell, Malden, MA.

Tape, W., and C. Tape (2012), A geometric setting for moment tensors, *Geophys. J. Int.*, *190*, 476–498, doi:10.1111/j.1365-246X.2012.05491.x.

VanDecar, J. C., and R. S. Crosson (1990), Determination of teleseismic relative phase arrival times using multi-channel cross-correlation and least squares, *Bull. Seismol. Soc. Am.*, *80*(1), 150–169.

Walker, C. C., J. N. Bassis, H. A. Fricker, and R. J. Czerwinski (2013), Structural and environmental controls on Antarctic ice shelf rift propagation inferred from satellite monitoring, *J. Geophys. Res. Earth Surface*, *118*, 2354–2364, doi:10.1002/2013JF002742.

Walter, F., J. F. Clinton, N. Deichmann, D. S. Dreger, S. E. Minson, and M. Funk (2009), Moment tensor inversions of icequakes on Gornergletscher, Switzerland, *Bull. Seismol. Soc. Am.*, *99*(2A), 852–870, doi:10.1785/0120080110.

Walter, F., D. S. Dreger, J. F. Clinton, N. Deichmann, and M. Funk (2010), Evidence for near-horizontal tensile faulting at the base of Gornergletscher, a Swiss Alpine Glacier, *Bull. Seismol. Soc. Am.*, *100*(2), 458–472, doi:10.1785/5012090083.

Wiens, D. A., J. J. McGuire, P. J. Shore, M. G. Bevis, K. Draunidalo, G. Prasad, and S. P. Helu (1994), A deep earthquake aftershock sequence and implications for the rupture mechanism of deep earthquakes, *Nature*, *372*, 540–543.

Wiens, D. A., S. Anandakrishnan, J. P. Winberry, and M. A. King (2008), Simultaneous teleseismic and geodetic observations of the stick-slip motion of an Antarctic ice stream, *Nature*, *453*, 770–775, doi:10.1038/nature06990.

Xu, Y., K. D. Koper, O. Sufri, L. Zhu, and A. R. Hutko (2009), Rupture imaging of the M_w 7.9 12 May 2008 Wenchuan earthquake from back projection of teleseismic P waves, *Geochem. Geophys. Geosyst.*, *10*, Q04006, doi:10.1029/2008GC002335.

Young, N. W., and G. Hyland (2002), Velocity and strain rates derived from InSAR analysis over the Amery Ice Shelf, East Antarctica, *Ann. Glaciol.*, *34*, 228–234.